PHYSICAL REVIEW B **104**, 245123 (2021)

Wood's anomaly beyond the Meixner-Schäfke theorem: Analytical and experimental investigation of sinusoidally modulated metasurfaces with normal susceptibilities

Amit Shaham *[*]* and Ariel Epstein *[†]*
Andrew and Erna Viterbi Faculty of Electrical and Computer Engineering, Technion–Israel Institute of Technology, Haifa 3200003, Israel

(Received 19 September 2021; revised 25 November 2021; accepted 1 December 2021; published 14 December 2021)

We present a rigorous analysis of plane-wave-illuminated sinusoidally modulated metasurfaces (MSs) with normal susceptibility components, without limiting the modulation-index values. In contrast to tangentially polarizable scenarios, which are treated within the conventional continued-fraction framework of Meixner and Schäfke, the unconventional structure of the generalized sheet transition conditions with regard to normal components manifests exotic stability conditions, which were not addressed by this framework. By introducing small losses into the constituents of such MSs (inevitable in practice), we resolve these stability issues and establish a valid solution for the scattered fields. Such solutions reveal that for a certain range of modulations these surfaces feature a resonant absorptive notch at an angle related to the period, associated with strong coupling to the weakly evanescent first-order Floquet-Bloch harmonic. Based on our observations, we identify this phenomenon as Wood's anomaly for MSs with normal susceptibilities. We verify these observations numerically and experimentally using suitable, systematically designed, printed-circuit-board prototypes. This work highlights the fundamental intricacies involving theoretical analyses of inhomogeneous normally polarizable MSs and constitutes a firm ground for further exploration and utilization of nonuniform configurations with these mostly ignored degrees of freedom.

DOI: 10.1103/PhysRevB.104.245123

I. INTRODUCTION

Wave propagation in periodic structures manifests many fundamental phenomena, which have aided studying and controlling the features of electromagnetic, optical, acoustic, and matter (de Broglie) waves, ever since the dawn of modern science [1–6]. Particularly, in electromagnetism and optics, the properties of dielectric and metallic periodic configurations, such as diffraction gratings, stratified bulks, periodically loaded waveguides, periodic impedance surfaces, photonic crystals, and artificial metamaterials, have been extensively investigated and exploited in a wide variety of applications, including filters, polarizers, resonators, transducers, superlenses, and slow-wave structures for particle beams and antennas [3,4,6,7].

Among all forms of periodicity, the sinusoidal modulation constitutes a relatively simple yet essential subclass to investigate. Compared to general periodic modulations, which may be expressed in terms of Fourier series, the sinusoidal modulation merely contains the offset and the fundamental harmonic of the series. Therefore, the latter is typically convenient to analyze, especially as a principal case study from which fundamental properties can be deduced and applied in more advanced configurations. As such, several electromagnetic configurations with spatial sinusoidal modulation were thoroughly analyzed in the past, mainly in aspect of their dispersion properties, band structures, and eigenmode compositions [1,3,8–11]. An important demonstration for the analysis of sinusoidally modulated structures was carried out by Hessel and Oliner [12], who rigorously addressed reactance surfaces with general periodic modulations in order to explain the empirically discovered Wood's anomalies [13,14], and satisfactorily demonstrated their results using a sinusoidally modulated case study.

Conceptually, the reactance surfaces analyzed in [3,8,12] can be viewed as a subclass of metasurfaces (MSs). Metasurfaces are thin planar arrangements of engineered subwavelength scatterers, such that the electric and magnetic dipoles induced upon them reradiate prespecified scattered fields. They have been extensively studied throughout the past few decades for their ability to efficiently manipulate electromagnetic wave fronts [15–17]. The compactness and low loss of MSs make them notable candidates for implementation of modern microwave and optical applications: enhanced antennas, thin lenses, unconventional reflectors, polarizers, filters, and cloaking, to name but a few [15,16].

Owing to the vanishing thickness of MSs and the subwavelength interparticle spacing upon them, one may homogenize the aforementioned individual dipoles into macroscopic distributions of surface electric ($\vec{P}_{\mathrm{s}}$) and magnetic ($\vec{M}_{\mathrm{s}}$) polarizations. Such polarizations inflict tangential field discontinuities across the MS, as formulated by the generalized sheet transition conditions (GSTCs) [18–20]. Furthermore, for linear MSs, the induced polarizations are related to the driving electromagnetic fields via four 3×3 surface susceptibility tensors ($\overline{\overline{\chi}}$) determined by the constituents and geometry of the MS. Once carefully engineered, the field discontinuities across the MS uniquely determine the scattered fields everywhere via the equivalence principle [17,21].

Over the past two decades or so, these GSTCs [18–20] were utilized to analyze and synthesize MSs for a wide

---

[*] samitsh@campus.technion.ac.il
[†] epsteina@ee.technion.ac.il

variety of applications. For example, it has been shown that collocated electric and magnetic susceptibilities are necessary to allow reflectionless anomalous refraction, also known as Huygens' MSs [22–24]; for wide-angle beam steering, a more elaborated structure turned out to be required, including bianisotropic response of the omega type [25–28]; and for advanced polarization manipulations, bianisotropic chiral inclusions were found to be of use [29–31]. Particularly, based on the analysis in [8], sinusoidally modulated MSs were recently integrated in MS leaky-wave antennas [32–35].

A closer look at the GSTCs [18–20] reveals that *tangential gradients of normal polarizations* generate tangential field discontinuities across the MS, as equally well as *tangential polarizations*. Thus, in order to implement a specific desired field transformation, it is sufficient to introduce only the latter (and discard the former). Following this notion, the mainstream framework for MS analysis and synthesis, e.g., as in [22–31], which typically considers MS functionality or reactance requirements only at a single incidence scenario, adopted utilization of *tangential* (in-plane) susceptibilities while mostly ignoring the *normal* (out-of-plane) components. The rationale behind such a choice is that implementation of a desired tangential-polarizations profile is expected to be less cumbersome than the alternative gradient profile of their normal counterparts [36,37].

This gives rise to the question of whether such equivalence between tangential and normal *polarizations* ($\vec{P}_{\rm s}$ and $\vec{M}_{\rm s}$) passes on, in a sense, to the *susceptibilities* ($\overline{\overline{\chi}}$). In this context, it was recently shown by Albooyeh *et al.* [37] that when a single obliquely incident plane-wave scenario is considered, normal susceptibilities may indeed be replaced with equivalent tangential components to achieve the same response for the same incident-field configuration. However, when multiple incidence scenarios are considered, results from the same report and from other reports, e.g., [38–41], indicate that tangential and normal susceptibilities are distinguishable. For example, Zaluški *et al.* [38] managed to separate between the characterization of the tangential and normal components of a macroscopically uniform MS by measuring its scattering parameters at *two different angles of incidence*.

Therefore, one may directly deduce that normal susceptibilities constitute separate and independent degrees of freedom which hold the potential to enhance MS functionalities, especially with respect to multiangular and spatially dispersive designs. In fact, implicit and explicit forms of normal susceptibilities were already suggested to stabilize the angular response of high impedance surfaces (HISs, also known as artificial magnetic conductors, AMCs) [42], Huygens' (reflectionless) MSs [43], and absorbers [44]. Furthermore, angular filters [45], spatially dispersive optical analog computing operations [46], and mimicry of nonreciprocal functionalities with reciprocal structures [39] were also implemented by embedding normal susceptibilities in MSs.

Be that as it may, the territory of normal susceptibilities remains mostly uncharted as far as *spatially modulated* MSs are concerned. Nevertheless, studying such structures is pertinent, seeing as spatial modulation is essential for the operation of many MS devices: lenses, anomalous reflectors and refractors, beam splitters, spatial light modulators, and so forth. Hence, embedding normal susceptibilities as additional degrees of freedom in such designs may provide them with augmented functionalities and performance, as well as facilitate and improve control over their angular response and spatial-dispersion properties.

In this paper, we address spatially modulated MSs with normal susceptibilities by analyzing and validating a principal case study: plane-wave scattering off MSs with sinusoidally modulated normal magnetic susceptibilities. Following previous studies, which effectively feature sinusoidally modulated *tangential* susceptibilities, e.g., [8,9,12], we apply conventional Floquet-Bloch (FB) analysis for the scattered fields (Sec. II A) and arrive at an infinite set of linear equations to be solved. In these past studies, [8,9,12], such sets of equations were treated using a particular mathematical theorem presented by Meixner and Schäfke [47] (henceforth referred to as the Meixner-Schäfke theorem), which guarantees a unique stable solution under certain conditions. Contrarily to such studies, our analysis reveals that the unconventional structure of the GSTCs with regard to *normal* components leads to scenarios for which the Meixner-Schäfke theorem is no longer valid, such that no stable solution can be formulated following standard procedures. We propose to overcome such stability issues by introducing small loss (unavoidable in practice) and amending the formula in the Meixner-Schäfke theorem to yield well-defined unique solutions for normal inclusions as well (Sec. II B).

To verify the fidelity of our theoretical predictions, we methodically synthesize realistic printed-circuit-board (PCB) MS prototypes (Sec. III A), and inspect them via full-wave simulations (Sec. III A) and experimental measurements after fabrication (Sec. III B). Our results exhibit a narrow resonant absorptive notch in the angular behavior of the fundamental FB harmonic (diffraction order) for vanishing offsets and small amplitudes of the modulation. We further show that the reason for such a phenomenon is strong coupling into the first order FB harmonic at the vicinity of its cutoff, upon transition from radiation to evanescence. We identify this result as a manifestation of Wood's anomalies [12–14], extending the scope of this evidently universal phenomenon to include normally polarizable MSs as well. We show that inclusion of other parasitic susceptibility components and fabrication nonidealities is essential for proper interpretation of the response of the realistic prototype, yielding good agreement between theory, full-wave, and experimental results.

Our theory and results regarding normally polarizable sinusoidally modulated MS, as presented in this paper, shed light on the uniqueness of normal components, which necessitate nontrivial treatment when incorporated in canonical problems, in addition to their distinct angular-dependence properties discussed earlier. Importantly, it points out a physical path to resolve instability issues in wave-grating scattering problems beyond the standard Meixner-Schafke theorem, revealing that the nonconventional normal susceptibility components support Wood's anomaly as well.

II. THEORY

A. Formulation

We consider a MS at $z = 0$, illuminated by a plane wave from below ($z < 0$). In the general scenario, such a MS may

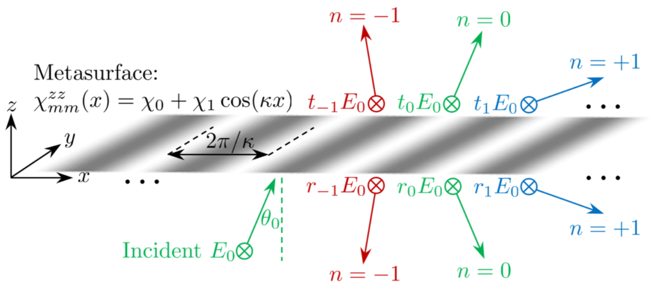

FIG. 1. Physical scattering configuration of a sinusoidally modulated MS with normal susceptibilities. An incident TE wave ("Incident E_0") impinges the sinusoidally modulated MS at $z=0$ and angle θ_0. Scattered FB harmonics are excited. Here only the $n=0,\pm1$ harmonics are visualized (as radiating).

possess both electric ($\vec{P}_\mathrm{s}$) and magnetic ($\vec{M}_\mathrm{s}$) polarizations, which are responsible for the tangential discontinuities of the electric ($\vec{E}$) and magnetic ($\vec{H}$) fields, as prescribed by the GSTCs [18–20],

$$\begin{aligned}\hat{z}\times(\vec{H}_\mathrm{t}^+-\vec{H}_\mathrm{t}^-)&=j\omega\vec{P}_\mathrm{st}-\hat{z}\times\vec{\nabla}_\mathrm{t}M_\mathrm{sz}\\(\vec{E}_\mathrm{t}^+-\vec{E}_\mathrm{t}^-)\times\hat{z}&=j\omega\mu\vec{M}_\mathrm{st}-\vec{\nabla}_\mathrm{t}\left(\frac{P_\mathrm{sz}}{\epsilon}\right)\times\hat{z}\end{aligned}\tag{1}$$

and

$$\begin{aligned}\vec{P}_\mathrm{s}&=\epsilon\overline{\overline{\chi}}_\mathrm{ee}\cdot\vec{E}^\mathrm{av}+c^{-1}\overline{\overline{\chi}}_\mathrm{em}\cdot\vec{H}^\mathrm{av},\\\vec{M}_\mathrm{s}&=\eta^{-1}\overline{\overline{\chi}}_\mathrm{me}\cdot\vec{E}^\mathrm{av}+\overline{\overline{\chi}}_\mathrm{mm}\cdot\vec{H}^\mathrm{av},\end{aligned}\tag{2}$$

where $\pm$ superscripts denote the fields as evaluated at $z\to0^\pm$; t and z subscripts denote components tangential and normal to the MS, respectively; av superscript denotes the average of the fields acting on the MS, i.e., $\vec{E}^\mathrm{av}=(\vec{E}^++\vec{E}^-)/2$ and $\vec{H}^\mathrm{av}=(\vec{H}^++\vec{H}^-)/2$; $\overline{\overline{\chi}}_\mathrm{ee}$, $\overline{\overline{\chi}}_\mathrm{mm}$, $\overline{\overline{\chi}}_\mathrm{em}$, and $\overline{\overline{\chi}}_\mathrm{me}$ are the electric, magnetic, electromagnetic, and magnetoelectric susceptibility tensors, respectively; ϵ, μ, c, and η are the standard constitutive parameters of the surrounding medium; and harmonic time dependence of $e^{j\omega t}$ is assumed and suppressed.

Herein, as we recall, we wish to focus on normal susceptibility components. In particular, we consider a sinusoidally modulated MS with normal magnetic susceptibility

$$\chi^{zz}_\mathrm{mm}(x)=\chi_0+\chi_1\cos(\kappa x),\tag{3}$$

where $\chi^{zz}_\mathrm{mm}(x)$ denotes the $\hat{z}\hat{z}$-dyad component of the magnetic susceptibility $\overline{\overline{\chi}}_\mathrm{mm}$, χ_0 is the offset of the modulation, χ_1 is its amplitude, and κ is its spatial frequency in units of radians divided by length, related to the modulation's spatial period $2\pi/\kappa$ (Fig. 1). All other susceptibility components are assumed to vanish. The MS is illuminated from $z<0$ with a y-polarized transverse-electric (TE) plane wave with θ_0 as the angle of incidence, described by $E_{y,\mathrm{inc}}(\vec{r})=E_0e^{-j(k_{x,0}x+k_{z,0}z)}$, where E_0 is the electric-field amplitude of the incident wave; $k_{x,0}=k\sin\theta_0$ and $k_{z,0}=k\cos\theta_0$ are the tangential and normal components of its wave vector (with respect to the MS); and $k=\omega\sqrt{\epsilon\mu}$ is the wave number in the surrounding medium.

Due to the periodicity of the MS, we may express the scattered fields everywhere as a superposition of FB harmonics [11,48,49]. Furthermore, the problem is y independent ($\partial_y=0$), hence, no transverse-magnetic polarized fields are scattered and the total electric field is y polarized:

$$E_y(\vec{r})=E_0\sum_{n=-\infty}^{\infty}e^{-jk_{x,n}x}\begin{cases}\delta_{n,0}e^{-jk_{z,0}z}+r_ne^{jk_{z,n}z} & z<0\\t_ne^{-jk_{z,n}z} & z>0,\end{cases}\tag{4}$$

where r_n and t_n are the yet-to-be-found reflection and transmission coefficients associated with the nth FB harmonic, respectively (see Fig. 1); $k_{x,n}=k_{x,0}+n\kappa$ and $k_{z,n}=\sqrt{k^2-k_{x,n}^2}$ are the tangential and normal wave-vector components associated with the nth FB harmonic, respectively (the radiation condition requires $\mathrm{Re}\{k_{z,n}\}>0$ and $\mathrm{Im}\{k_{z,n}\}<0$); and $\delta_{n,0}$ is the Kronecker delta, which corresponds to the incident wave. The magnetic fields may be obtained by applying Faraday's law on Eq. (4):

$$H_x(\vec{r})=-\frac{E_0}{k\eta}\sum_{n=-\infty}^{\infty}k_{z,n}e^{-jk_{x,n}x}\begin{cases}\delta_{n,0}e^{-jk_{z,0}z}-r_ne^{jk_{z,n}z} & z<0\\t_ne^{-jk_{z,n}z} & z>0\end{cases}\tag{5}$$

and

$$H_z(\vec{r})=\frac{E_0}{k\eta}\sum_{n=-\infty}^{\infty}k_{x,n}e^{-jk_{x,n}x}\begin{cases}\delta_{n,0}e^{-jk_{z,0}z}+r_ne^{jk_{z,n}z} & z<0\\t_ne^{-jk_{z,n}z} & z>0\end{cases}.\tag{6}$$

Therefore, once r_n and t_n are found for all $n\in\mathbb{Z}$, the scattered fields are known entirely via Eqs. (4)–(6).

For the MS defined by Eq. (3) and the TE field configuration in Eqs. (4)–(6), the GSTCs of Eqs. (1) and (2) reduce into

$$E_y^+=E_y^-,\quad H_x^+-H_x^-=-\partial_x\left[\chi^{zz}_\mathrm{mm}(x)\frac{H_z^++H_z^-}{2}\right].\tag{7}$$

We substitute the fields, Eqs. (4)–(6), at $z\to0^\pm$ in the GSTCs of Eq. (7). The continuity of the tangential electric field in Eq. (7) yields an inhomogeneous infinite set of linear equations

$$t_n=r_n+\delta_{n,0},\qquad\forall n\in\mathbb{Z};\tag{8}$$

while the discontinuity of the tangential magnetic field in Eq. (7) results, after some algebraic manipulations, in another inhomogeneous system of infinitely many linear equations,

$$\begin{aligned}(\delta_{n,0}-t_n-r_n)k_{z,n}={}&\frac{j\chi_0}{2}k_{x,n}^2(t_n+r_n+\delta_{n,0})\\&+\frac{j\chi_1}{4}k_{x,n-1}k_{x,n}(t_{n-1}+r_{n-1}+\delta_{n-1,0})\\&+\frac{j\chi_1}{4}k_{x,n+1}k_{x,n}(t_{n+1}+r_{n+1}+\delta_{n+1,0}),\end{aligned}\tag{9}$$

which should be satisfied for every $n\in\mathbb{Z}$. Substituting Eq. (8) in Eq. (9), we obtain

$$\begin{aligned}&\frac{j\chi_1}{2}k_{x,n}(k_{x,n+1}t_{n+1}+k_{x,n-1}t_{n-1})\ +(j\chi_0k_{x,n}^2+2k_{z,n})t_n\\&\quad=2k_{z,0}\delta_{n,0}.\end{aligned}\tag{10}$$

A canonical and more compact form of Eq. (10) reads

$$\tau_{n+1}-D_n\tau_n+\tau_{n-1}=\frac{4k_{z,0}\delta_{n,0}}{j\chi_1k_{x,0}}\quad\forall n\in\mathbb{Z},\tag{11}$$

where we define the normal magnetic field transmission coefficients [see Eq. (6)]

$$\tau_n = k_{x,n} t_n; \tag{12}$$

the canonical coefficient sequence

$$D_n = -\frac{2\chi_0}{\chi_1} + \frac{4jk_{z,n}}{\chi_1 k_{x,n}^2} \overset{\text{def}}{=} D_\infty + \frac{4jk_{z,n}}{\chi_1 k_{x,n}^2}; \tag{13}$$

and its asymptote $D_\infty = -\frac{2\chi_0}{\chi_1}$, the limit of D_n as $n \to \pm\infty$.

Given the sequence of canonical coefficients D_n, which is entirely determined by the parameters of the MS configuration in Eq. (3) and the incident plane wave (i.e., χ_0, χ_1, κ, k, and θ_0), our goal is to find a proper solution for the unknown sequence τ_n ($n \in \mathbb{Z}$) and, in turn, extract t_n and r_n using Eqs. (12) and (8). In fact, mathematically speaking, Eq. (11) constitutes a linear second-order recurrence relation with variable coefficients; as such, for each choice of an adequate initial-value set, $(\tau_0, \tau_1) \in \mathbb{C}^2$, one obtains a unique solution for all the elements of the sequence τ_n, by applying Eq. (11) recursively. As a consequence, infinitely many solutions exist for Eq. (11); yet, as inferred from Eqs. (6) and (12), it is necessary to seek for a solution with well-behaved (namely, stable, nondiverging) asymptotes as $n \to \pm\infty$, such that the FB series for H_z^+, as expressed in Eq. (6), converges properly.

Recurrence relations of the canonical form in Eq. (11) were extensively investigated in the past, as they occur in many physical and mathematical problems, especially in the analysis of wave propagation in sinusoidally stratified media [1,3,8,9,12,47,50]. In particular, it was shown by Meixner and Schäfke (Meixner-Schäfke theorem) [47] that if $\exists N \in \mathbb{N}$ such that $|D_n| \geqslant 2, \forall |n| > N$, then there exists a unique stable solution for Eq. (11) (i.e., $\tau_n \to 0$ for $|n| \to \pm\infty$), where τ_0/τ_1 is expressed in the form of a continued fraction.

Indeed, all conventional studies that involve such a form of recursive relations (e.g., as in [1,3,8,9,12,32–34,47,50], for which $|D_n| \to \infty$) rely on the Meixner-Schäfke theorem. In contrast, due to the unconventional structure of the GSTCs (1) with respect to the normal susceptibilities, the sequence $D_n = D_\infty + \frac{\mathcal{O}(n)}{\mathcal{O}(n^2)} \xrightarrow[n\to\pm\infty]{} D_\infty = -\frac{2\chi_0}{\chi_1}$ does not satisfy the Meixner-Schäfke theorem if the absolute value of the modulation index (χ_1/χ_0) is greater than unity (the modulation index is not limited in this analysis). More specifically, in our study, the spatial derivative operator ∂_x in Eq. (7), which did not appear in conventional problems, such as [8], operates twice on the tangential electric field E_y [since in addition to the explicit ∂_x operator written in Eq. (7), the normal magnetic field is evaluated via $H_z = -\frac{\partial_x E_y}{\omega\mu}$], and eventually manifests itself in the denominator in Eq. (13). This directly stems from the inherent nonlocality of the normal (magnetic) susceptibilities. Therefore, the conventional continued-fraction formula of the Meixner-Schäfke theorem [47] fails to converge (namely, unstable) if one naively plugs Eq. (13) into it. This will be further discussed in the following subsection.

B. Semianalytical converging solution

In what follows, we propose a path to overcome the instability issues encountered in the previous section. In order to devise a way that would lead to a stable solution of Eqs. (11) and (13) nonetheless, we inspect the asymptote of Eq. (11) for large $n > 0$ by approximating D_n as D_∞ therein. This asymptote is then described via a homogeneous second-order difference equation with constant coefficients, which has two independent exponential solutions [51],

$$\tau_n^\pm = (\alpha_\pm)^n, \tag{14}$$

where

$$\alpha_\pm = \frac{D_\infty \pm \sqrt{D_\infty^2 - 4}}{2} \tag{15}$$

are the roots of the characteristic equation

$$\alpha^2 - D_\infty \alpha + 1 = 0. \tag{16}$$

Vietta's formulas state that $\alpha_+\alpha_- = 1$ in this case, leading to two possible scenarios: (i) one of the roots $\alpha_\pm$ has less-than-unity magnitude [exponential decay, stable, as indicated by Eq. (14)], while the other has greater-than-unity magnitude (exponential growth, unstable); and (ii) both the roots have unity magnitudes (oscillatory, unstable). From Eq. (15), for the lossless case ($\chi_0, \chi_1, D_\infty \in \mathbb{R}$), scenario (i) occurs for $|D_\infty| > 2$ and (ii) occurs for $|D_\infty| < 2$, in consistency with the condition required for the Meixner-Schäfke theorem [47].

The key for obtaining a stable solution is the introduction of small losses in the constituents of our model, an essential physical property of any practical system. Such inclusion of losses (even if infinitesimal) is mandatory in many physical models, which are otherwise described by excessively idealistic mathematical formulations that lead to ill-defined results. In the context of our problem, such consideration of losses constitutes the heart of the uniqueness theorem for time-harmonic electromagnetic fields [21], which relies on the presence of (at least) infinitesimal losses in the overall medium.

Hence, in order to arrive at well-defined solutions for unlimited modulation-index values (e.g., $\chi_0 \to 0$, as we consider later herein), we resolve the instability issue in case (ii) above by introducing small loss, ensuring that one of the roots in Eq. (15) of the asymptote in Eq. (16), denoted hereafter by $\tilde{\alpha}$, is always stable as in case (i) above.

For example, let us consider a particular scenario of small losses by introducing $\chi_0 = \chi_0' - j\chi_0''$, where $\chi_0' \in \mathbb{R}$ and $\chi_0'' > 0$ are the reactive (real) and lossy (imaginary) parts of the modulation offset χ_0, respectively. For simplicity and conciseness we retain χ_1 as real and positive, set $\chi_0' = 0$ (i.e., only lossy part in the offset), and assume small losses $\chi_0'' \ll \chi_1$. Then $D_\infty = -\frac{2\chi_0}{\chi_1} = \frac{2j\chi_0''}{\chi_1}$ [see Eq. (13)] and Eq. (15) becomes

$$\alpha_\pm = -j\left[\sqrt{1+\left(\frac{\chi_0''}{\chi_1}\right)^2} \pm \frac{\chi_0''}{\chi_1}\right] \approx -j\left(1 \pm \frac{\chi_0''}{\chi_1}\right). \tag{17}$$

It is immediately seen that $|\alpha_+| > 1$ and $|\alpha_-| < 1$, in accordance with Vietta's formulas. Therefore, the stable root to be taken is $\tilde{\alpha} = \alpha_-$ in this case.

Next, to solve the scattering problem in practice, we denote $q_n = \tau_{n-1}/\tau_n$, $n \in \mathbb{N}\backslash\{0\}$. The recurrence relation of Eq. (11) becomes $q_n = D_n - 1/q_{n+1}$. Repeated substitutions yield terminated continued fractions as follows [47]:

$$\frac{\tau_0}{\tau_1} = q_1 = D_1 - \frac{1}{q_2} = D_1 - \frac{1}{D_2 - \frac{1}{q_3}}$$

$$= \cdots \;\; = D_1 - \frac{1\,|}{|D_2} - \cdots - \frac{1\,|}{|D_{m-1}} - \frac{1}{q_m}. \qquad (18)$$

For large values of m, we terminate Eq. (18) with the asymptote $q_m = \tau_{m-1}/\tau_m \to \tilde{\alpha}^{m-1}/\tilde{\alpha}^m = 1/\tilde{\alpha}$, where $\tilde{\alpha}$ is the aforementioned stable root of the asymptotic characteristic equation [Eq. (16)] when small loss is considered, and (semianalytically) obtain the ratio τ_0/τ_1. The corresponding ratio τ_0/τ_{-1} for the negative FB-harmonic indices ($n < 0$) of the sequence is obtained similarly by inspecting the sequence for $n \to -\infty$. These two ratios are then substituted in Eq. (11) with $n = 0$ to extract τ_0. With the values of τ_0 and q_1 at hand, one may obtain all the other unknowns (τ_n, t_n, and r_n) by applying the recurrence relation of Eq. (11) recursively: $\tau_1 = \tau_0/q_1$; $\tau_2 = D_1\tau_1 - \tau_0$; $\tau_3 = D_2\tau_2 - \tau_1$; and so forth.

At this point, an important observation regarding our method of solution should be emphasized for the completeness of our discussion. Many scattering and dispersion relations for periodic media ([3,8–12,52], for instance), which are analyzed using FB-harmonic expansions, are typically expressed via an infinite set of linear equations with infinitely many unknowns (namely, the FB harmonics' amplitudes) to be solved. Such equation sets can be represented in infinite-matrix form. Specifically, in our analysis, the matrix form of Eq. (11) is

$$\begin{bmatrix} \ddots & & & & \vdots & & & \iddots \\ & 1 & -D_{-1} & 1 & 0 & 0 & & \\ \cdots & 0 & 1 & -D_0 & 1 & 0 & \cdots \\ & 0 & 0 & 1 & -D_1 & 1 & & \\ \iddots & & & & \vdots & & & \ddots \end{bmatrix} \cdot \begin{bmatrix} \vdots \\ \tau_{-1} \\ \tau_0 \\ \tau_1 \\ \vdots \end{bmatrix}$$

$$= \begin{bmatrix} \vdots \\ 0 \\ \frac{4k_{z,0}}{j\chi_1 k_{x,0}} \\ 0 \\ \vdots \end{bmatrix}. \qquad (19)$$

To solve Eq. (19) and extract the coefficients τ_n as desired, one might be tempted to employ truncation and inversion, as conventionally performed in such problems, e.g., as in [11,52]. However, such truncation, say into a $2N+1$ by $2N+1$ system, in other words, keeping only the $-N \leqslant n \leqslant N$ elements of τ_n and $-N \leqslant n \leqslant N$ equations of the equation set Eq. (11), tacitly enforces $\tau_n = 0$ for every $|n| > N$. Consequently, this imposes the termination of $1/q_{N+1} = \tau_{N+1}/\tau_N = 0$ in Eq. (18) (for nontrivial solutions), in contrast to the termination condition $1/q_{N+1} = \tilde{\alpha}$, which was just shown to be the only choice leading to a stable solution.

Therefore, although the typical truncation methodology works well for many cases, it should be used with care, since it may lead to solution divergence in some scenarios (such as the one considered herein, for instance). In addition, in case of uncertainty with regard to the convergence rate, applying truncation and inversion to Eq. (19) might invoke time-consuming inversions of large matrices. In contrast, our method of stable-root terminated continued fractions, as formulated in Eq. (18), merely requires a sequence of relatively simple arithmetic calculations, and results in an exponentially decaying sequences of amplitudes τ_n and t_n, which guarantee the absolute and uniform convergence of the FB sums in Eqs. (4)–(6) into meaningful and physical values.

In conclusion, the resolution of the nonrealistic lossless scenario with the introduction of physically inevitable dissipation establishes a fast converging and robust semianalytical method for analyzing sinusoidally modulated MSs with normal susceptibilities.

III. RESULTS AND DISCUSSION

A. Design and full-wave validation

To validate the theoretical analysis and demonstrate it in practice, we design two PCB MS prototypes, operating at 20 GHz. Following standard MS synthesis schemes [17], the abstract constituent distribution, Eq. (3), should be discretized into subwavelength intervals, and suitable scatterer geometries (meta atoms), locally implementing the required response, should be devised. Thus, we first focus on designing the general meta-atom structure, and associating specific geometrical parameters with effective magnetic susceptibility (lookup table). Subsequently, to construct the entire MS, we place the various meta-atoms in their respective locations to implement the stipulated modulation profile $\chi_{\mathrm{mm}}^{zz}(x)$ [Eq. (3)], using the lookup table (LUT) to replace the abstract susceptibility with a physical structure.

1. Meta-atom design and characterization

We focus first on the preparatory design process of the individual meta atoms to be used. Following [19], the local magnetic response of each meta atom is implemented by a subwavelength, capacitively loaded printed copper loop with out-of-plane magnetic dipole moment [Fig. 2(a)]. When z-directed magnetic field is applied, circumventing currents in the loop are induced, giving rise to an effective magnetic dipole (magnetic polarization), as desired.

The overall dimensions of each unit cell accommodating the loop is $L_x \times L_y$, where $L_x = L_y = 3$ mm $\approx 0.2\lambda$ ($\lambda \approx 15$ mm is the wavelength in the vacuum surroundings at 20 GHz); $t_{\mathrm{sub}} = 0.127$ mm is the thickness of the commercial Rogers RO3003$^{\mathrm{TM}}$ substrate, chosen for the implementation, with relative dielectric permittivity of $\epsilon_{\mathrm{sub}} = 3$ and loss tangent of 0.001; $a = 0.85$ mm is the outer radius of the printed copper loops; $t = 0.08$ mm is the traces' width; $g = 0.08$ mm is the separation between the printed capacitors' strips, compatible with standard PCB fabrication limitations; and W is the capacitors' width, by which the local susceptibility value of the meta atom $\chi_{\mathrm{mm}}^{zz}(x)$ is yet to be controlled.

Owing to the subwavelength dimensions of each loop, we approximately model its response via an equivalent quasistatic lumped circuit, excited by the time-varying flux of the normal magnetic field H_z [19] [Fig. 2(b)]. The induced electromotive force generates a corresponding current flow I along the loop, which is inversely proportional to the total impedance of the equivalent circuit. The resultant normal magnetic dipole moment of the individual loop, which is proportional to this

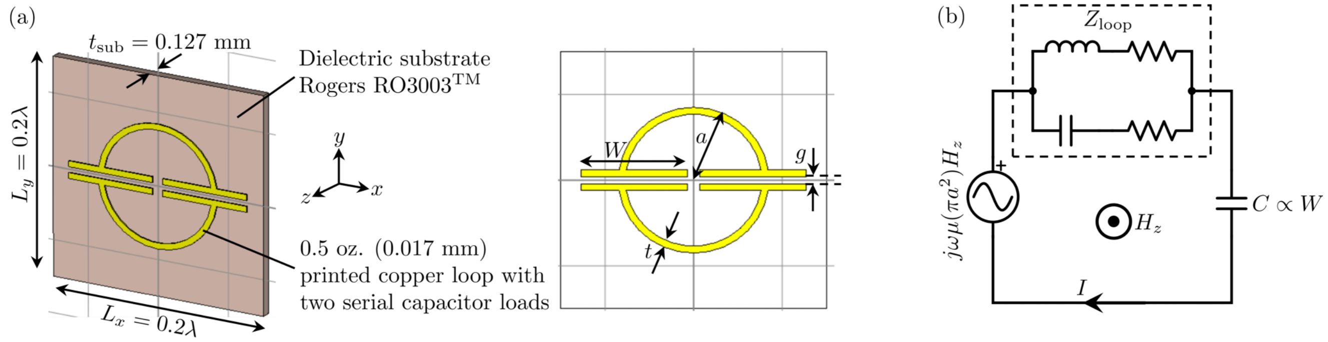

FIG. 2. (a) Perspective (left) and top (right) views of a typical meta atom as designed in CST along with relevant dimensions. (b) Simple quasistatic circuit approximation for the meta atoms in (a): the normal magnetic field H_z induces electromotive force along the loop via Faraday's law $[j\omega\mu(\pi a^2)H_z]$. The resultant current I upon the loop is then determined by the reactive impedance of the loop ($Z_{\rm loop}$) in series with the load capacitance C. In turn, the magnetic dipole moment is generated, which is proportional to I. Following such analysis, the meta atom's local susceptibility $\chi_{\rm mm}^{zz}$ approximation, Eq. (20), is obtained (see Appendix A)

current, is then used to deduce the effective local value of the normal magnetic polarization distribution M_{sz}; the normal magnetic susceptibility value $\chi_{\rm mm}^{zz}$ of such meta atoms may thus be evaluated (see Appendix A).

This practically means that the magnetic susceptibility $\chi_{\rm mm}^{zz}$ of the loaded-loop meta atom can be controlled via the total impedance of the equivalent circuit in Fig. 2(b) (this notion will soon be exploited). In our design, this total impedance is comprised of the loop's impedance $Z_{\rm loop}$ in series with the $(j\omega C)^{-1}$ reactance of the equivalent load capacitance C due to both printed capacitors. The impedance $Z_{\rm loop}$ is determined by the fixed dimensions and electromagnetic properties of the loop and the substrate, as well as the frequency [19,53,54], whereas the load capacitance C (two identical capacitors in series) is approximately proportional to the width W [55–57], by which the local susceptibility value of the meta atom is eventually controlled. The loop's dimensions, a and t, are intentionally fixed such that $Z_{\rm loop}$ is inductive at 20 GHz (accompanied by undesired, yet inevitable, small resistance due to copper and dielectric losses). In this situation, one may access a wide range of positive and negative susceptibility values[1] at 20 GHz by carefully tuning the capacitors' width W close to the series LC resonance of the circuit. Overall, this model yields the following approximate relation between the real (reactive) part of the loop's susceptibility and the capacitors' width:

$$\mathrm{Re}\{\chi_{\rm mm}^{zz}\} \approx \frac{\beta W(1-\gamma W)}{(1-\gamma W)^2 + (\delta W)^2}, \tag{20}$$

where β, γ, and δ are constants determined from the electrical and geometrical properties of the substrate, loop, and capacitors, as well as the frequency of operation (see Appendix A and Ref. [19] for more details).

In order to realize accurate susceptibility values for the implementation of the sinusoidal modulation in Eq. (3), we characterized and fine-tuned our meta atoms at 20 GHz with the help of the commercial full-wave solver "CST Microwave Studio" (CST), as prescribed in [38]: for each value of W we arranged the meta atom in Fig. 2(a) in a macroscopically uniform planar MS configuration (by enforcing periodic boundary conditions in CST) and calculated the complex plane-wave reflection and transmission coefficients at incidence angles of 0° and 30°; from these scattering parameters, we extracted the normal magnetic $\chi_{\rm mm}^{zz}$ [Fig. 3(a)] and tangential electric $\chi_{\rm ee}^{yy}$ [Fig. 3(b), regarded as negligible for the moment] components, as formulated in [38]. Copper and dielectric losses were taken into account in these simulations and all the other simulations that follow; the lossy part (imaginary part of the susceptibilities) obtained from the characterization will be discussed in the next subsection.

Since the full-wave simulations tend to be time consuming at the vicinity of the meta atom's LC resonance, we performed the simulation for several values of W which yield moderate $\mathrm{Re}\{\chi_{\rm mm}^{zz}\}$ values, and fitted the plot to the analytical approximation of Eq. (20), by extracting the least-square-error values of β, γ, and δ, using `cftool` (curve-fitting tool) in the commercial computing platform MATLAB [Fig. 3(a)].[2] In this manner a reliable LUT with sufficient resolution and accuracy is established for the entire set of the loaded-loop meta atoms [Fig. 3(a)], enabling us to proceed towards constructing the sinusoidally modulated prototypes.

2. Sinusoidally modulated prototype design and full-wave validation

As mentioned in the beginning of Sec. III A, we proceed with the established LUT to the macroscopic design [17] of two sinusoidally modulated PCB MS prorotypes (Fig. 4): we discretize the desired normal magnetic susceptibility profile in Eq. (3) and arrange the loaded-loop meta atoms in accordance with the discretized profile; the capacitors' width W for the meta atom in each site is determined by utilizing the LUT obtained in Fig. 3(a). The prototypes are designed with the same

---

[1] Here we mean a wide range of positive and negative values for the real (reactive) part of the magnetic susceptibility. The imaginary (lossy) part will be discussed separately.

[2] The obtained least-square-error values for the meta atoms in Fig. 2(a) at 20 GHz and characterization [38] at 0° and 30° are $\beta \approx 48.24 \times 10^{-3}\ k^{-1}\ \mathrm{mm}^{-1}$, $\gamma \approx 0.8511\ \mathrm{mm}^{-1}$, and $\delta \approx 7.137 \times 10^{-3}\ \mathrm{mm}^{-1}$.

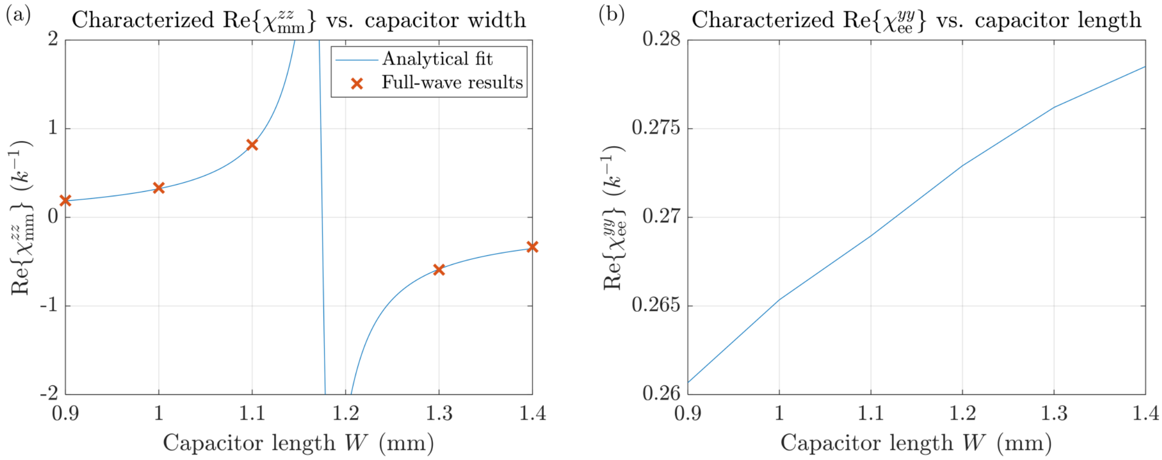

FIG. 3. (a) Characterized real part of the magnetic susceptibility $\mathrm{Re}\{\chi_{\mathrm{mm}}^{zz}\}$ vs the capacitors' width W for the meta-atom configuration in Fig. 2(a) at 20 GHz: full-wave results (orange x markers) and analytical fit following Eq. (20) (solid blue line). (b) Full-wave characterized real part of the electric susceptibility $\mathrm{Re}\{\chi_{\mathrm{ee}}^{yy}\}$ for the meta atom in Fig. 2(a) vs capacitors' width W at 20 GHz.

goal values of $\chi_0 = 0$ and $\chi_1 = 0.7k^{-1}$ for the modulation's offset and amplitude, and different spatial-variation rates of $\kappa/k = 1/2$ and $\kappa/k = 5/8$. One period of each prototype, as constructed in CST, is shown in Figs. 4(a) and 4(b); the chosen capacitors' width W and local real part of the susceptibility $\mathrm{Re}\{\chi_{\mathrm{mm}}^{zz}(x)\}$ of each meta atom in both designs are summarized in Table I. For these specific capacitor widths chosen to realize our prototypes, we also characterized the imaginary (lossy) part of the magnetic susceptibility $\mathrm{Im}\{\chi_{\mathrm{mm}}^{zz}(x)\}$, by using the process in [38] again; although the values vary slightly between meta atoms, they all remain around $\mathrm{Im}\{\chi_{\mathrm{mm}}^{zz}(x)\} \approx -0.01k^{-1}$ order of magnitude, which is used as an effective mean (offset) value in our theoretical calculations for these prototypes. Periodic boundary conditions were enforced in the simulation and a plane wave was launched towards each prototype with θ_0 incidence angle (as illustrated in Fig. 1), whose value was swept between 0° and 80°.

The fractions of power coupled to the specular reflection ($|r_0|^2$) and direct transmission ($|t_0|^2$) of the zeroth-order FB harmonic at 20 GHz are presented in Figs. 5(a) and 5(b) for these two prototypes, comparing the semianalytical predictions for the goal parameters $\chi_0 = 0$ (the small lossy part of $\chi_0'' = -\mathrm{Im}\{\chi_0\} = 0.01k^{-1}$, as previously characterized, is added to arrive at the stable solution discussed in Sec. II B) and $\chi_1 = 0.7k^{-1}$ with the numerical full-wave results of the prototypes in Fig. 4. We first observe that the MS is transparent for near-normal incidence (θ_0 values close to 0) and highly reflective at near-grazing illumination (θ_0 close to 90°). This observation is explained by the vanishing normal magnetic field for near-normal impingement, such that negligible normal magnetic polarization takes place [38]. Furthermore, a sharp angular notch, which manifests substantial reflectance and absorption, appears at a certain angle $\tilde{\theta}$, which, by virtue of these results, is seen to strongly depend on the spatial variation rate κ.

In order to shed light on the notch phenomenon, let us take a closer look at Eqs. (13) and (18) with vanishing offset ($\chi_0 = 0$) and small amplitude values (χ_1) of the modulation. In this case, D_∞ vanishes and the elements of D_n, which are inversely proportional to χ_1, attain large magnitudes, which decay as n increases towards the limit $D_\infty = 0$ [Eq. (13)]. The larger the spatial variation rate κ, the faster the decay rate of the sequence D_n with respect to n, and the faster the convergence of the sequence q_n to its limit $1/\tilde{\alpha}$ [due to the rapid growth of

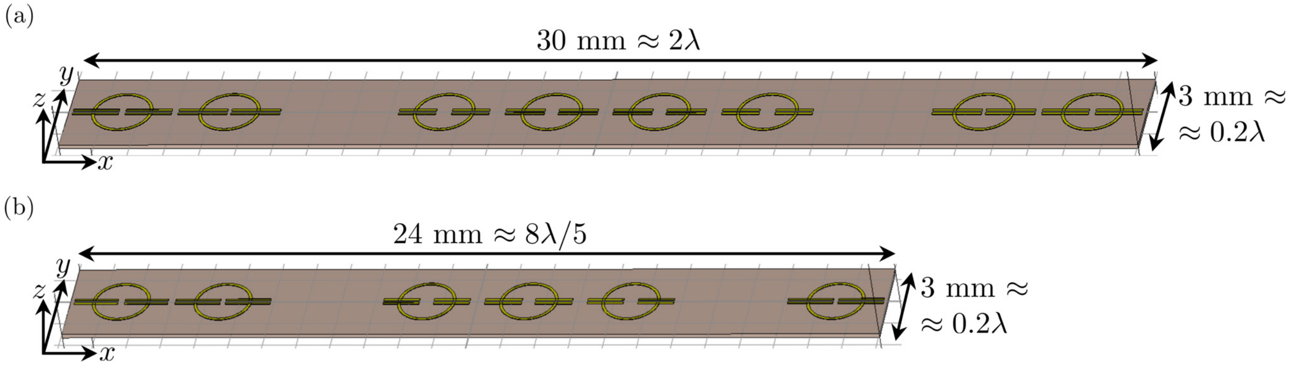

FIG. 4. One period of the PCB version for the (a) $\kappa/k = 1/2$ and (b) $\kappa/k = 5/8$ prototypes, as modeled in CST. The goal parameters for the modulation are $\chi_0 = 0$, $\chi_1 = 0.7k^{-1}$. The chosen capacitors' width W and local susceptibility χ_{mm}^{zz} of each meta atom in both designs are summarized in Table I.

TABLE I. Chosen capacitor lengths W and corresponding local susceptibility values χ_{mm}^{zz} [according to the LUT in Fig. 2(c)] for both the sinusoidally modulated MS prototypes designed in Figs. 4(a) and 4(a). The values are ordered from left to right in correspondence with the meta-atom arrangements in Fig. 4. "N/A" meta atoms refer to sites where no loaded loops are placed (only substrate), realizing vanishing susceptibilities (to a very good approximation).

Prototype	$\kappa/k = 1/2$		$\kappa/k = 5/8$	
Meta-atom no.	W (mm)	$\chi_{\mathrm{mm}}^{zz}(k^{-1})$	W (mm)	$\chi_{\mathrm{mm}}^{zz}(k^{-1})$
1 (leftmost)	1.283	−0.6657	1.277	−0.7
2	1.362	−0.4114	1.326	−0.495
3	N/A	0	N/A	0
4	1.033	0.4114	1.055	0.495
5	1.084	0.6657	1.088	0.7
6	1.084	0.6657	1.055	0.495
7	1.033	0.4114	N/A	0
8	N/A	0	1.326	−0.495
9	1.362	−0.4114		
10	1.283	−0.6657		

$k_{x,n}^2$ in the denominator of Eq. (13)], recalling that $\tilde{\alpha} \approx -j$ for the low-loss vanishing-offset scenario [Eq. (17)].

Thus, in view of Eq. (13) and its behavior for the range of parameters discussed herein ($\chi_0 = 0$, small χ_1, and moderate κ values, which lead to large values and moderate decay rate of the sequence D_n), we may approximate $\tau_0/\tau_1 \approx D_1$, i.e., keep the dominant term in Eq. (18). At the notch angle $\tilde{\theta}$, we expect the direct transmission to fall drastically. This corresponds to $\tau_0 \approx 0$, hence, the notch angle $\tilde{\theta}$ can be estimated from this relation by setting $\tau_0/\tau_1 \approx 0$, i.e., $D_1 \approx 0$. These steps result in the requirement $k_{z,1} \approx 0$ [see Eq. (13)] at the notch angle, which yields $\sin\tilde{\theta} \approx 1 - \kappa/k$ (provided that $\kappa/k < 1$). Following this analytical approximation yields 30° for $\kappa/k = 1/2$ [Fig. 5(a)] and 22.02° for $\kappa/k = 5/8$ [Fig. 5(b)], which agrees very well with the semianalytical results, $\tilde{\theta} \approx 30.2°$ and $\tilde{\theta} \approx 22.2°$, respectively.

The requirement $k_{z,1} \approx 0$ (also called the Rayleigh wavelength of the first-order FB harmonic [12,58]) implies that at the notch angle the first-order FB harmonic is weakly evanescent (i.e., on the verge of radiation, close to its cutoff), while the resulting condition $\tau_0/\tau_1 \approx 0$ implies that the amplitude of electric field $|t_1|$ coupled into this mode is large. This phenomenon is further demonstrated in Fig. 5(c), which shows the semianalytical predictions of the *field* transmission ($|t_1|$) and reflection ($|r_1|$) coefficients' magnitudes into the first-order FB harmonic vs angle of incidence for the $\kappa/k = 1/2$ prototype. These magnitudes attain their large maximal value exactly at the notch angle, where the strong coupling into this confined surface mode (and other high-order modes) is

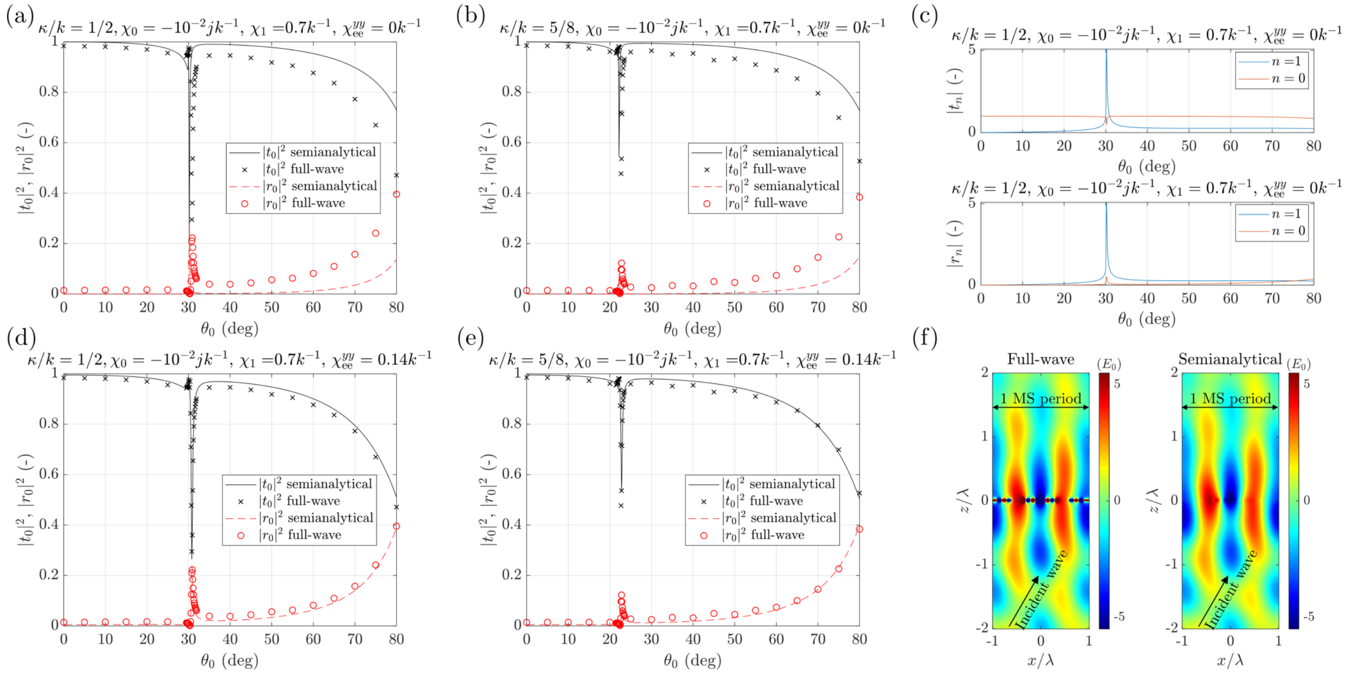

FIG. 5. (a),(b) Semianalytical predictions following Eq. (18) with $\chi_{\mathrm{ee}}^{yy} = 0$ (black solid and red dashed lines) compared to full-wave simulation results (black x and red circle markers) of the zeroth-order FB harmonic power scattering coefficients, $|r_0|^2$ (red dashed line and circle markers) and $|t_0|^2$ (black solid line and x markers) in linear scale, vs incidence angle for the two prototypes of Fig. 4 ($\chi_0 = -0.01jk^{-1}$ and $\chi_1 = 0.7k^{-1}$), differing by their spatial modulation rate (a) $\kappa/k = 1/2$ and (b) $\kappa/k = 5/8$. (c) Semianalytical field transmission and reflection coefficients into the $n = 0, 1$ FB harmonics in linear scale for the $\kappa/k = 1/2$ prototype ($\chi_{\mathrm{ee}}^{yy} = 0$), exhibiting strong coupling into the $n = 1$ harmonic around its transition between radiation and evanescence (at the notch angle). (d) $\kappa/k = 1/2$ and (e) $\kappa/k = 5/8$ prototypes zeroth-order FB harmonic power scattering coefficients ($|r_0|^2$ and $|t_0|^2$ in linear scale) vs incidence angle, compared with the extended analytical model that also includes constant tangential electric susceptibility $\chi_{\mathrm{ee}}^{yy} = 0.14k^{-1}$ (see Appendix B). (f) Real part of the electric-field phasor at the vicinity of the $\kappa/k = 1/2$ MS on the $y = 0$ plane, for illumination at its notch angle $\theta_0 = 30.8°$; left: full-wave results with the prototype from Fig. 4(a); right: semianalytical predictions following the analysis elaborated on in Appendix B with $\chi_{\mathrm{ee}}^{yy} = 0.14k^{-1}$.

responsible for the substantial dissipation of power in the MS (typically few tens of percent).

Similar phenomena of sharp fluctuations in transmittance or reflectance were observed in the past, for example by Wood [13,14], which empirically noticed "unexpected" narrow dark bands in the spectrum of an optical diffraction grating illuminated by white light (widely known as Wood's anomalies). The phenomenon was later explained by Hessel and Oliner [12], who presented a thorough scattering analysis for plane-wave-illuminated periodically modulated impedance sheets (which feature, in effect, tangential susceptibility components). Upon investigation of their obtained scattering equation, Hessel and Oliner revealed that the underlying phenomena behind the dark bands observed by Wood are, in fact, forced resonances of the impedance surface. These resonances occur when the incident wave's real-valued transverse wave number (denoted herein as $k_{x,0}$) is close to one of the complex-valued transverse wave numbers of the surface's leaky-wave eigenmodes. In particular, they have further shown that for vanishing offsets of the constituents' modulation, the nth resonance, associated with the nth leaky-wave eigenmode, occurs exactly under the same condition derived herein: $k_{z,n} \approx 0$. Indeed, as is clear from these similarities, the notch phenomenon observed in Fig. 5 is yet another type of Wood's anomaly, shown herein to occur also in MSs with *normal* susceptibilities (compared to previous reports, which regard tangentially polarizable scenarios), thus further highlighting the universal nature of this physical phenomenon.

In addition to the angular trend of the prototypes, we observe that the qualitative behavior of the simulated results is similar to that of the analytical predictions, yet certain quantitative discrepancies can be observed between the two scattering coefficients' magnitudes. These discrepancies can be explained by the fact that the loop meta atoms possess additional electric and bianisotropic susceptibility components [19] [see Fig. 3(b)]. These additional components mainly stem from the azimuthal asymmetry of the loops due to the load capacitors (compared to unloaded closed loops, for instance): these asymmetries give rise to non-negligible higher-order nonuniform spatial harmonics in the current distribution along each loop (even when their dimensions are subwavelength) and lead to charge accumulation, which effectively manifests parasitic electric dipole moment [19,53,54].

In order to probe this hypothesis, we incorporated additional constant (x- and y- independent) electric susceptibility component χ_{ee}^{yy} into the analytical model (Appendix B) and swept its values, seeking the best fit between the analytical and full-wave results. The best match occurs at $\chi_{\mathrm{ee}}^{yy} = 0.14k^{-1}$, for both prototypes [Figs. 5(d) and 5(e)]. This *effective* value is comparable to the ones extracted for the individual meta atoms in Fig. 3(b). The difference between the former and the latter values implies that other factors may also contribute to the discrepancies seen in Figs. 5(a) and 5(b), such as (small) bianisotropic components possessed by the loop [19], which are not considered in our model and the characterization process [38]; small variations in local susceptibility values due to different adjacent-cell coupling when the MS is no longer uniform; and discretization errors. Nevertheless, excellent agreement is observed between theory and simulation [Figs. 5(d) and 5(e)] when effective dominant electric susceptibility is considered [as implied by Fig 3(b)]. Overall, Figs. 5(a) and 5(b) clearly show that the main qualitative features of the original model predictions are still retained, even with the slight nonideality of the practical implementation.

To conclude our full-wave validation, we compare between the semianalytical predictions [calculated via Eq. (4) with the parasitic $\chi_{\mathrm{ee}}^{yy} = 0.14k^{-1}$ evaluated above] and full-wave results obtained for the real part of the tangential electric field $\mathrm{Re}\{E_y(\vec{r})\}$ on the $y = 0$ plane [Fig. 5(f)]. In this demonstration, a plane wave impinges the $\kappa/k = 1/2$ prototype at the notch angle $\theta_0 = 30.8^\circ$ [Fig. 5(d)] for both the full-wave simulation and semianalytical calculation. A dominant surface wave with periodicity that corresponds to that of the first-order FB harmonic is evident, in agreement with the results in Fig. 5(c) and the physical interpretation following Wood's anomaly. Excellent agreement between the fields' distributions is noticeable (despite the high sensitivity of the MS response near the resonant notch), which serves as another support for the fidelity of the analytical model, succeeding in accurate reproduction of the scattering phenomena around the surface.

At this point, we may already conclude that our extension to the semianalytical Meixner-Schäfke theorem [47] for normal-susceptibility scenarios yields accurate and reliable results, as evident from the very good overall correspondence with the full-wave simulations.

B. Experimental verification

In order to experimentally verify our theoretical observations, both PCB prototypical designs from Fig. 4 were printed on a commercial 9 × 12-in. ($\approx 15.24\lambda$ in the uniform y direction and $\approx 20.32\lambda$ in the sinusoidally modulated x direction) Rogers RO3003$^{\mathrm{TM}}$ laminates by PCB Technologies Ltd., Migdal Haemek, Israel [Figs. 6(a) and 6(b)], and experimentally characterized in the anechoic chamber at the Technion [Figs. 6(c) and 6(d)]. Each prototype was mounted on a rotatable foam holder, placed approximately at the focus of a Gaussian-beam antenna (Millitech Inc., GOA-42-S000094, focal distance of 196 mm $\approx 13\,\lambda$), illuminating the device under test (DUT) with a quasiplanar wave front. A planar near-field measurement system (MVG/Orbit-FR) was used to record the forward scattering pattern, by scanning an area of 400 mm ($\approx 26.6\lambda$) in the y direction over 400 mm in the x direction, at a distance of $z = 220$ mm from the center of the MS plane, from which the far-field pattern can be deduced using the equivalence principle [21]. After determining the angle of incidence θ_0 by rotation of the foam holder, an 18.5–20-GHz sweep was performed, accompanied by a reference measurement, for which the MS was removed and the Gaussian-beam antenna directly illuminated the same near-field scanning plane. By repeating this procedure for a set of angles θ_0 covering the desired characterization range, the angular response of the MS can be obtained.

The maximal far-field gain, calculated from the near-field measurements and calibrated with respect to the reference measurement (thus, representing the power fraction coupled into the direct transmission of the fundamental FB harmonic $|t_0|^2$), is presented as a function of the angle of incidence θ_0 for both MSs at several representative frequencies in

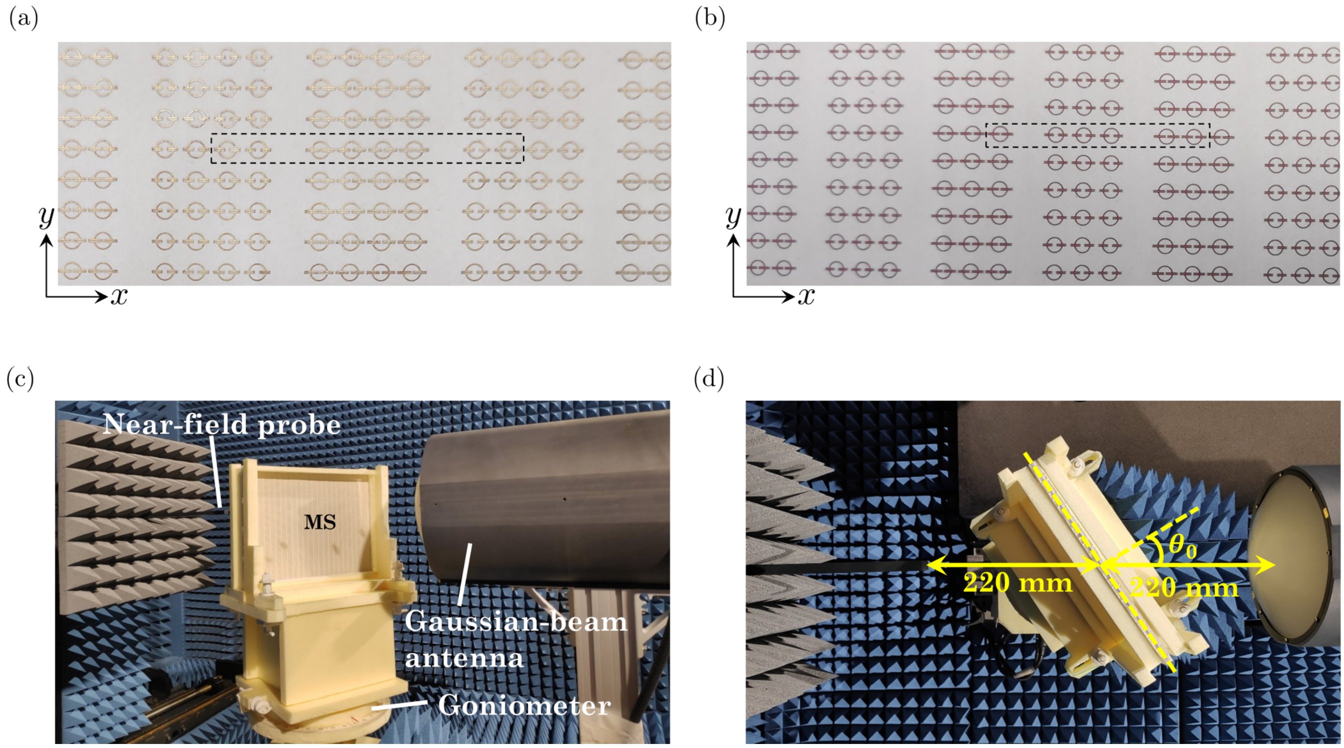

FIG. 6. Close view of the fabricated (a) $\kappa/k = 1/2$ and (b) $\kappa/k = 5/8$ MSs; the dashed black rectangles in (a) and (b) capture one period of the MS, as designed in Figs. 4(a) and 4(b), respectively. (c) Perspective view of the experimental setup: the MS is approximately located at the focus of the Gaussian-beam illumination from the antenna, while the near-field probe performs a planar scan. (d) Top view of the experimental setup. The angle of incidence θ_0 is set with the help of a goniometer with 0.5° resolution.

Fig. 7, in comparison to the analytical predictions presented in Figs. 5(c) and 5(d). The experimental results for both MSs show shallow and spread drop in the transmitted power around a certain, frequency-dependent angle, accompanied by a steep rolloff at grazing incidence angles for ∼18.5–19 GHz, and a deeper and less spread frequency-dependent drop, followed by a moderate rolloff at grazing angles for ∼19–19.75 GHz. At higher frequencies the drop completely disappears and the MS exhibits only rolloff behavior.

Although the measured response at the intended frequency of operation (20 GHz) does not fit well to our theoretical predictions, better correspondence is observed at slightly lower

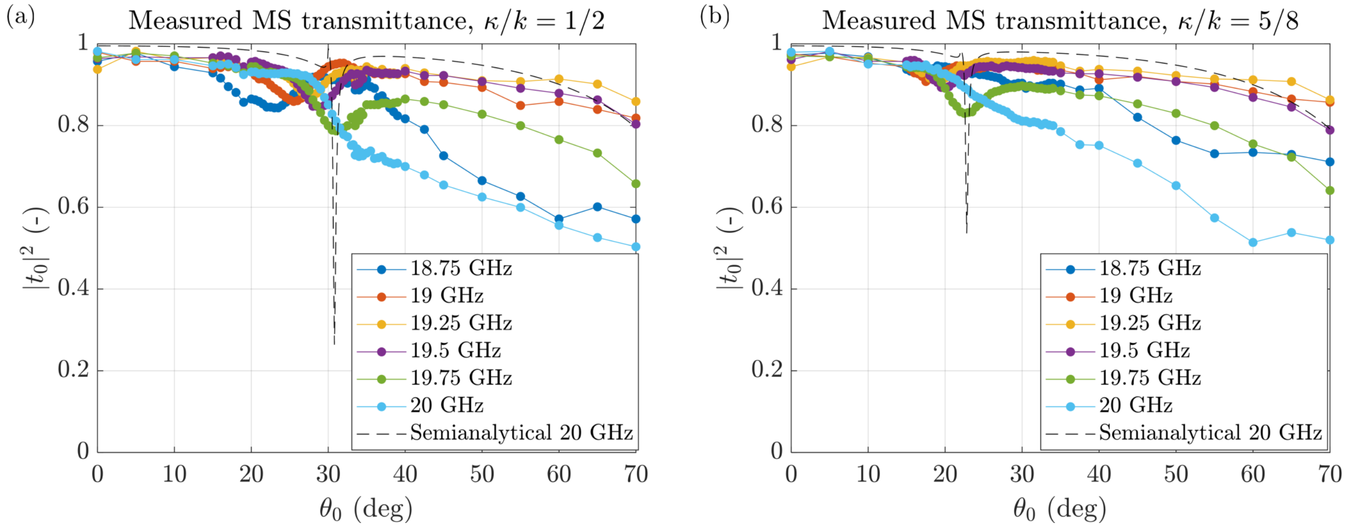

FIG. 7. Measured far-field transmittance in linear scale vs the angle of incidence (colored solid lines with full circles) for the (a) $\kappa/k = 1/2$ and (b) $\kappa/k = 5/8$ prototypes for several frequencies: $f = 18.75$ GHz (blue), $f = 19$ GHz (red), $f = 19.25$ GHz (orange), $f = 19.5$ GHz (purple), $f = 19.75$ GHz (green), and $f = 20$ GHz (cyan). The dashed black "Semianalytical 20 GHz" traces show the semianalytical predictions [Figs. 5(c) and 5(d)] of the infinite periodic MSs designed in Fig. 4 and illuminated by a 20-GHz plane wave.

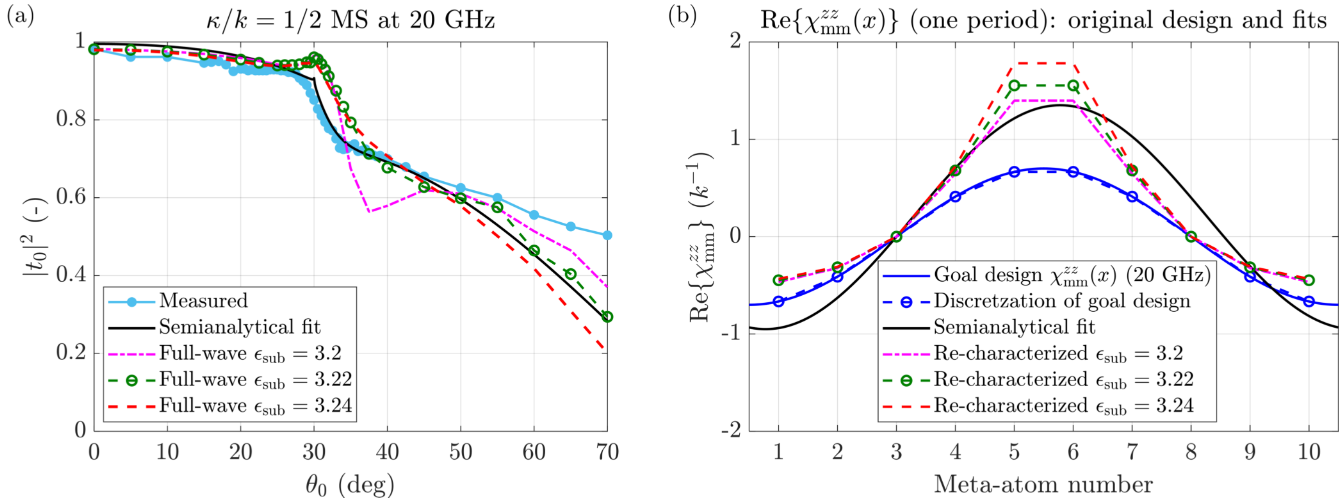

FIG. 8. (a) Zeroth-order FB-harmonic transmittance in linear scale of the $\kappa/k = 1/2$ prototype vs the incident angle, as compared between the experimental 20-GHz results (cyan solid line with full circles); full-wave 20-GHz simulations with different substrate permittivities $\epsilon_{\mathrm{sub}} = 3.2$ (magenta dot-dashed line), $\epsilon_{\mathrm{sub}} = 3.22$ (green dashed line with circles), and $\epsilon_{\mathrm{sub}} = 3.24$ (red dashed line); and modified semianalytical predictions with $\chi_0 = (0.2 - 0.1j)k^{-1}$, $\chi_1 = 1.15k^{-1}$, and $\chi_{\mathrm{ee}}^{yy} = 0.14k^{-1}$ (black solid line). (b) Real part of the local magnetic susceptibility values χ_{mm}^{zz} of the meta atoms as arranged on the $\kappa/k = 1/2$ prototype in Fig. 4(a): goal sinusoidal modulation ($\chi_0 = 0$ and $\chi_1 = 0.7k^{-1}$, blue solid line) and its discretization (blue dashed line with circles), best-fit sinusoidal modulation ($\mathrm{Re}\{\chi_0\} = 0.2k^{-1}$, $\chi_1 = 1.15k^{-1}$, black solid line), and resultant local values for modified substrate permittivities ϵ_{sub} [other dashed and dot-dashed lines in correspondence with (a) herein].

frequencies (19.75 GHz, green trace, 1.25% relative frequency shift): one can clearly identify a drop occurring at the expected angle of incidence (with the theoretical notch) for both κ values consistently. Nonetheless, the measured drops are shallower and wider than those expected according to the theoretical analysis.

Seeing as possible fabrication tolerances and inaccuracies may inflict deviations of the measurements from the theoretical predictions, we probed the influence of certain parameter variations in our design on the MS response. One such factor that may affect our results, as was also suggested in [59], is a possible variation in the substrate's permittivity ϵ_{sub} with respect to the nominal values provided by the manufacturer. Based on the realistic estimations of up to ±10% deviation in ϵ_{sub}, as reported in [59,60], we investigate the dependence of the $\kappa/k = 1/2$-prototype [Fig. 4(a)] response on such variations at 20 GHz. It is expected that such variations, even if moderate, would cause non-negligible discrepancies in the local meta atoms' susceptibilities [e.g., via the deviations of the capacitance values C in Eq. (20)], due to their proximity to resonance, as inferred by Fig. 3(a). Since the resultant deviation of the susceptibility values most likely leads to spatial variations which are not precisely sinusoidally modulated, full-wave simulations of the model in Fig. 4(a) were applied in this investigation for the sake of accuracy.

A comparison between the experimental and full-wave results for the values of $\epsilon_{\mathrm{sub}} = 3.2$, 3.22 and 3.24 (instead of the originally specified nominal value $\epsilon_{\mathrm{sub}} = 3$) is presented in Fig. 8(a). Despite the high sensitivity of the MS transmittance at large angles with respect to the substrate's permittivity ϵ_{sub} at this range of values, good agreement is observed between the measured and full-wave results with $\epsilon_{\mathrm{sub}} = 3.22$.

To examine the possible extent of such susceptibility variations, which may lead to the effects exhibited by the experimental measurements, we swept the χ_0 and χ_1 values of the analytical model, seeking for the effective values that yield the best agreement between the semianalytical (with $\chi_{\mathrm{ee}}^{yy} = 0.14k^{-1}$) and experimental results for the $\kappa/k = 1/2$ prototype at 20 GHz. Even though the fabricated MS is not likely to remain precisely sinusoidally modulated at 20 GHz, the effective values of $\chi_0 = (0.2 - 0.1j)k^{-1}$ and $\chi_1 = 1.15k^{-1}$ [leading to the black profile plotted in Fig. 8(b)], compared to the original $\chi_0 = 0$ and $\chi_1 = 0.7k^{-1}$ [blue profiles in Fig. 8(b)], achieve good agreement between the results, as shown by the black trace in Fig. 8(a).

In view of this fit, one may ask whether the permittivity shifts which were pointed out as a possible cause for the measured scattering coefficients can indeed affect the meta-atom susceptibilities in a such a manner. To examine this, we re-extracted the individual meta-atom properties, as discussed in Sec. III A (using [38] and CST simulations again), for the various substrate permittivities considered in Fig. 8(a). Figure 8(b) shows these re-characterized values *in situ* [with respect to the prototype in Fig. 4(a)] and compares them with the effective sinusoidal modulation obtained from our semianalytical investigation (black trace), as well as the original goal values of the modulation (blue traces). Indeed, plausible correspondence can be observed, especially at the larger positive values around the peak of the modulation, which seem to play the dominant part in the overall response of the MS.

It is important to note that the value of $\epsilon_{\mathrm{sub}} = 3.22$, which leads to best agreement between theory and measurement, is, in fact, an *effective* value which may account for other possible realistic fabrication tolerances (e.g., deviations in the substrate's thickness or printed-traces' dimensions), which may very well cause substantial disturbance to the surface susceptibility profiles in a way that can explain the general trends seen in the measurements.

In summary, our experimental results (Fig. 7, 19.75 GHz) show qualitative agreement between theory and measurements, especially in aspects of drop (or notch) angle and overall trend. Subject to reasonable realistic manufacturing errors (physically supported by the semianalytical model), especially when considering the sensitive near-resonance design, good congruence is simultaneously observed between theory, simulations, and experimental measurements.

IV. CONCLUSION

To conclude, we have presented and validated a rigorous, robust, and fast-converging methodology for scattering analysis of a fundamental case study of spatially modulated MSs with normal susceptibilities: sinusoidally modulated MSs with normal magnetic susceptibilities. Importantly, we have shown that it is essential to include physically inevitable losses in the constituents of such MSs in order to enable valid solutions for the scattered fields. Such extensions of the Meixner-Schäfke theorem could be readily adopted in other physical problems of sort, or utilized to treat more complex meta-atom configurations (involving bianisotropic components, for instance, or more general periodic modulations).

In addition, we thoroughly validated this theory and proposed an elaborate practical PCB-compatible design scheme, supported by standard manufacturing process of etching commercial laminates. We identified Wood's anomalies for normally polarizable MSs, which retain their universal resonant-notch nature for this scenario as well (i.e., not restricted to tangentially polarizable configurations, which were analyzed in previous reports). The numerical and experimental results are well explained, both semianalytically and with full-wave simulations, within the bounds of plausible manufacturing inaccuracies, despite the challenging resonant behavior and susceptibility imperfection of the meta atoms in practice. On the other hand, such increased sensitivity to the close surrounding exhibited by this kind of MSs may prove advantageous in applications of sensing [61]. This analysis of the possible measurement errors emphasizes the importance and usefulness of the analytical model, which provides a convenient and insightful way of probing the effects of the various physical parameters on the behavior of the MS.

Overall, this work can be viewed as a significant step towards better clarifying the role of normal susceptibilities and their integration in more elaborated configurations, enabling solutions also for devices which do not obey the Meixner-Schäfke theorem conditions, aiming at harnessing these unique and often-overlooked degrees of freedom in advanced designs.

ACKNOWLEDGMENTS

The authors gratefully acknowledge Rogers Corporation for providing the laminates used in this study. They would also like to thank Y. Komarovsky of the Communication Laboratory in the Faculty of Electrical and Computer Engineering at the Technion for his technical assistance with regard to the experimental setup. A.S. also thanks Dr. S. W. Marcus and O. Rabinovich of the META group at the Technion for fruitful discussions.

APPENDIX A: DESIGN CONSIDERATIONS AND ELABORATED CIRCUIT ANALYSIS FOR THE LOADED-LOOP META ATOMS

In this Appendix we summarize the main steps and considerations of the the meta atoms' design process at 20 GHz (see [19] for more details). First, in order to achieve the maximal inductance from each loop, we set the trace width as $t = 0.08$ mm (which is slightly wider than the fabrication-process limitation of minimal 3-mil trace and gap widths). Then, in order to minimize the undesired susceptibility components of the loop (mainly χ_{ee}^{yy} and $\chi_{\mathrm{em}}^{yz} = -\chi_{\mathrm{me}}^{zy}$) we sought the minimal possible value for the outer radius of the loop ($a = 0.85$ mm) that maintains sufficiently large inductance. Such a radius would allow a wide enough range of positive and negative $\mathrm{Re}\{\chi_{\mathrm{mm}}^{zz}\}$ values via reasonable (i.e., contained inside the unit-cell boundaries) widths of the printed capacitors W [by tuning the serial LC resonance of the loaded lumped loop, as described in Fig. 3(a)].

By sweeping the printed capacitors' width W, one effectively controls the meta atom's local susceptibility via the total series impedance of the loaded loop [see Fig. 2(b)]. Following [19] and the equivalent lumped-circuit model in Fig. 2(b), an approximate expression for χ_{mm}^{zz} is given by

$$\begin{aligned}\chi_{\mathrm{mm}}^{zz} &\approx \frac{\mu_0\omega^2(\pi a^2)^2}{L_xL_y}\frac{C}{j\omega C Z_{\mathrm{loop}}+1}\\ &= \frac{\mu_0\omega^2(\pi a^2)^2}{L_xL_y}\frac{C}{j\omega C(R_{\mathrm{loop}}+jX_{\mathrm{loop}})+1},\end{aligned}\tag{A1}$$

where a, L_x, and L_y are the dimensions of the meta atom specified in Fig. 2(a); C is the total load capacitance implemented by the two printed capacitors (in series); and $Z_{\mathrm{loop}} = R_{\mathrm{loop}} + jX_{\mathrm{loop}}$ is the lumped impedance of the loop, where its real and imaginary parts, R_{loop} and X_{loop}, are, in principle, determined from the geometrical and electrical parameters of the loop and the dielectric substrate for the frequency of operation ω [19]. The relation between the load capacitance C (two identical capacitors in series) and the width W is approximately linear [55–57]: $C/W \approx 6.9\epsilon_{\mathrm{eff}}$ (fF/mm); where ϵ_{eff} is the effective value of the relative dielectric constant experienced by the loop and the capacitors. Thus, the real (reactive) part of χ_{mm}^{zz} in (A1) as a function of the capacitors' width W has the approximate form of

$$\begin{aligned}\mathrm{Re}\{\chi_{\mathrm{mm}}^{zz}\} &\approx \frac{\mu_0\omega^2(\pi a^2)^2}{L_xL_y}\frac{C(1-\omega X_{\mathrm{loop}}C)}{(1-\omega X_{\mathrm{loop}}C)^2+(\omega R_{\mathrm{loop}}C)^2}\\ &\overset{\mathrm{def}}{=} \frac{\beta W(1-\gamma W)}{(1-\gamma W)^2+(\delta W)^2},\end{aligned}\tag{A2}$$

where $\beta = 6.9\times10^{-12}\mu_0\epsilon_{\mathrm{eff}}\omega^2(\pi a^2)^2/(L_xL_y)$, $\gamma = 6.9\times10^{-12}\omega\epsilon_{\mathrm{eff}}X_{\mathrm{loop}}$ [m^{-1}], and $\delta = 6.9\times10^{-12}\omega\epsilon_{\mathrm{eff}}R_{\mathrm{loop}}$ (m^{-1}). For the sake of accuracy, the values of β, γ, and δ were retrieved via full-wave simulations as described in Sec. III A.

APPENDIX B: INCORPORATION OF CONSTANT TANGENTIAL ELECTRIC SUSCEPTIBILITY χ_{ee}^{yy} INTO THE MODEL

In this Appendix we show the main steps for the incorporation of constant electric susceptibility χ_{ee}^{yy} into the model introduced in Sec. II. The magnetic susceptibility $\chi_{\rm mm}^{zz}(x)$ and the expression for the fields $\vec{E}(\vec{r})$ and $\vec{H}(\vec{r})$ remain as defined in Eqs. (3) and (4)–(6), respectively. On the other hand, the GSTCs are modified into

$$E_y^+ = E_y^-,\quad H_x^+ - H_x^- = -\partial_x\left[\chi_{\rm mm}^{zz}(x)\frac{H_z^+ + H_z^-}{2}\right] + j\omega\epsilon\chi_{\rm ee}^{yy}\left[\frac{E_y^+ + E_y^-}{2}\right]. \tag{B1}$$

We repeat the same process executed in Sec. II and substitute Eqs. (4)–(6) in Eq. (B1). After some algebraic manipulations we obtain Eq. (8) and

$$\frac{j\chi_1}{2}k_{x,n}(k_{x,n+1}t_{n+1} + k_{x,n-1}t_{n-1}) + (j\chi_0 k_{x,n}^2 + jk^2\chi_{\rm ee}^{yy} + 2k_{z,n})t_n = 2k_{z,0}\delta_{n,0}, \tag{B2}$$

which should be satisfied for every $n \in \mathbb{Z}$. Clearly, Eq. (B2) reduces into Eq. (10) when $\chi_{\rm ee}^{yy} = 0$ (i.e., when no electric susceptibility is considered). Defining $\tilde{\tau}_n = k_{x,n}t_n$ and manipulating Eq. (B2) yield

$$\tilde{\tau}_{n+1} - \tilde{D}_n\tilde{\tau}_n + \tilde{\tau}_{n-1} = \frac{4k_{z,0}\delta_{n,0}}{j\chi_1 k_{x,0}},\quad \forall n \in \mathbb{Z}, \tag{B3}$$

where

$$\tilde{D}_n = -\frac{2\chi_0}{\chi_1} + \frac{4jk_{z,n} - 2k^2\chi_{\rm ee}^{yy}}{\chi_1 k_{x,n}^2}. \tag{B4}$$

To evaluate the coupling to the various scattered modes, the same procedure shown in Sec. II B is readily performed for $\tilde{\tau}_n$ with the simple replacement of D_n by $\tilde{D}_n$. In particular, since the limit of $\tilde{D}_n$ as $|n| \to \infty$ is still $D_\infty = -\frac{2\chi_0}{\chi_1}$, small loss is added to the magnetic susceptibility in this scenario as well, in order for a stable root $\tilde{\alpha}$ of the asymptote in Eq. (16) to exist.

[1] L. Brillouin, *Wave Propagation in Periodic Structures: Electric Filters and Crystal Lattices*, 2nd ed. (Dover, New York, 1953).

[2] N. W. Ashcroft and N. D. Mermin, *Solid State Physics* (Saunders College Publishing, Orlando, 1976).

[3] C. Elachi, Waves in active and passive periodic structures: A review, Proc. IEEE **64**, 1666 (1976).

[4] E. Yablonovitch, Photonic crystals, J. Mod. Opt. **41**, 173 (1994).

[5] M. I. Hussein, M. J. Leamy, and M. Ruzzene, Dynamics of phononic materials and structures: Historical origins, recent progress, and future outlook, Appl. Mech. Rev. **66**, 040802 (2014).

[6] F. Capolino, *Theory and Phenomena of Metamaterials* (CRC, Boca Raton, Florida, 2009).

[7] X. Zhang and Z. Liu, Superlenses to overcome the diffraction limit, Nat. Mater. **7**, 435 (2008).

[8] A. Oliner and A. Hessel, Guided waves on sinusoidally-modulated reactance surfaces, IRE Trans. Antennas Propag. **7**, 201 (1959).

[9] T. Tamir, H. C. Wang, and A. A. Oliner, Wave propagation in sinusoidally stratified dielectric media, IEEE Trans. Microwave Theory Tech. **12**, 323 (1964).

[10] A. Hessel, M. H. Chen, R. C. M. Li, and A. A. Oliner, Propagation in periodically loaded waveguides with higher symmetries, Proc. IEEE **61**, 183 (1973).

[11] P. S. J. Russell, Optics of Floquet-Bloch waves in dielectric gratings, Appl. Phys. B **39**, 231 (1986).

[12] A. Hessel and A. A. Oliner, A new theory of Wood's anomalies on optical gratings, Appl. Opt. **4**, 1275 (1965).

[13] R. Wood, XLII. On a remarkable case of uneven distribution of light in a diffraction grating spectrum, London, Edinburgh, Dublin Philos. Mag. J. Sci. **4**, 396 (1902).

[14] R. W. Wood, Anomalous diffraction gratings, Phys. Rev. **48**, 928 (1935).

[15] S. B. Glybovski, S. A. Tretyakov, P. A. Belov, Y. S. Kivshar, and C. R. Simovski, Metasurfaces: From microwaves to visible, Phys. Rep. **634**, 1 (2016).

[16] H.-T. Chen, A. J. Taylor, and N. Yu, A review of metasurfaces: Physics and applications, Rep. Prog. Phys. **79**, 076401 (2016).

[17] A. Epstein and G. V. Eleftheriades, Huygens metasurfaces via the equivalence principle: Design and applications, J. Opt. Soc. Am. B **33**, A31 (2016).

[18] M. Idemen, Universal boundary relations of the electromagnetic field, J. Phys. Soc. Jpn. **59**, 71 (1990).

[19] S. Tretyakov, *Analytical Modeling in Applied Electromagnetics* (Artech House, Boston, 2003).

[20] E. F. Kuester, M. A. Mohamed, M. Piket-May, and C. L. Holloway, Averaged transition conditions for electromagnetic fields at a metafilm, IEEE Trans. Antennas Propag. **51**, 2641 (2003).

[21] C. A. Balanis, *Advanced Engineering Electromagnetics* (John Wiley & Sons, Hoboken, NJ, 2012).

[22] C. Pfeiffer and A. Grbic, Metamaterial Huygens' Surfaces: Tailoring Wave Fronts with Reflectionless Sheets, Phys. Rev. Lett. **110**, 197401 (2013).

[23] F. Monticone, N. M. Estakhri, and A. Alù, Full Control of Nanoscale Optical Transmission with a Composite Metascreen, Phys. Rev. Lett. **110**, 203903 (2013).

[24] M. Selvanayagam and G. V. Eleftheriades, Discontinuous electromagnetic fields using orthogonal electric and magnetic currents for wavefront manipulation, Opt. Express **21**, 14409 (2013).

[25] J. P. S. Wong, A. Epstein, and G. V. Eleftheriades, Reflectionless wide-angle refracting metasurfaces, IEEE Antennas Wirel. Propag. Lett. **15**, 1293 (2016).

[26] V. S. Asadchy, M. Albooyeh, S. N. Tcvetkova, A. Díaz-Rubio, Y. Ra'di, and S. A. Tretyakov, Perfect control of reflection and refraction using spatially dispersive metasurfaces, Phys. Rev. B **94**, 075142 (2016).

[27] A. Epstein and G. V. Eleftheriades, Arbitrary power-conserving field transformations with passive lossless omega-type bianisotropic metasurfaces, IEEE Trans. Antennas Propag. **64**, 3880 (2016).

[28] A. Epstein and G. V. Eleftheriades, Synthesis of Passive Lossless Metasurfaces using Auxiliary Fields for Reflectionless

Beam Splitting and Perfect Reflection, Phys. Rev. Lett. **117**, 256103 (2016).

[29] Y. Zhao, M. Belkin, and A. Alù, Twisted optical metamaterials for planarized ultrathin broadband circular polarizers, Nat. Commun. **3**, 870 (2012).

[30] C. Pfeiffer, C. Zhang, V. Ray, L. J. Guo, and A. Grbic, High Performance Bianisotropic Metasurfaces: Asymmetric Transmission of Light, Phys. Rev. Lett. **113**, 023902 (2014).

[31] C. Pfeiffer and A. Grbic, Bianisotropic Metasurfaces for Optimal Polarization Control: Analysis and Synthesis, Phys. Rev. Appl. **2**, 044011 (2014).

[32] A. M. Patel and A. Grbic, A printed leaky-wave antenna based on a sinusoidally-modulated reactance surface, IEEE Trans. Antennas Propag. **59**, 2087 (2011).

[33] G. Minatti, F. Caminita, M. Casaletti, and S. Maci, Spiral leaky-wave antennas based on modulated surface impedance, IEEE Trans. Antennas Propag. **59**, 4436 (2011).

[34] M. Esquius-Morote, J. S. Gómez-Díaz, and J. Perruisseau-Carrier, Sinusoidally modulated graphene leaky-wave antenna for electronic beamscanning at THz, IEEE Trans. Terahertz Sci. Technol. **4**, 116 (2014).

[35] M. Faenzi, G. Minatti, D. González-Ovejero, F. Caminita, E. Martini, C. Della Giovampaola, and S. Maci, Metasurface antennas: New models, applications and realizations, Sci. Rep. **9**, 10178 (2019).

[36] K. Achouri, M. A. Salem, and C. Caloz, General metasurface synthesis based on susceptibility tensors, IEEE Trans. Antennas Propag. **63**, 2977 (2015).

[37] M. Albooyeh, D.-H. Kwon, F. Capolino, and S. A. Tretyakov, Equivalent realizations of reciprocal metasurfaces: Role of tangential and normal polarization, Phys. Rev. B **95**, 115435 (2017).

[38] D. Zaluški, A. Grbic, and S. Hrabar, Analytical and experimental characterization of metasurfaces with normal polarizability, Phys. Rev. B **93**, 155156 (2016).

[39] C. Pfeiffer and A. Grbic, Emulating Nonreciprocity with Spatially Dispersive Metasurfaces Excited at Oblique Incidence, Phys. Rev. Lett. **117**, 077401 (2016).

[40] K. Achouri and C. Caloz, Controllable angular scattering with a bianisotropic metasurface, in *2017 IEEE International Symposium on Antennas and Propagation USNC/URSI National Radio Science Meeting* (IEEE, San Diego, California, 2017), pp. 1489–1490.

[41] K. Achouri and O. J. F. Martin, Angular scattering properties of metasurfaces, IEEE Trans. Antennas Propag. **68**, 432 (2020).

[42] S. M. Hashemi, S. A. Tretyakov, M. Soleimani, and C. R. Simovski, Dual-polarized angularly stable high-impedance surface, IEEE Trans. Antennas Propag. **61**, 4101 (2013).

[43] Y. Ra'di and S. A. Tretyakov, Angularly-independent huygens' metasurfaces, in *2015 IEEE International Symposium on Antennas and Propagation USNC/URSI National Radio Science Meeting* (IEEE, Vancouver, British Columbia, Canada, 2015), pp. 874–875.

[44] S.-K. Tseng, H.-H. Hsiao, and Y.-P. Chiou, Wide-angle wide-band polarization-insensitive perfect absorber based on uniaxial anisotropic metasurfaces, Opt. Mater. Express **10**, 1193 (2020).

[45] J. D. Ortiz, J. P. del Risco, J. D. Baena, V. Losada, F. Medina, and J. L. Araque, Metasurfaces for angular filtering and beam scanning, in *2014 8th International Congress on Advanced Electromagnetic Materials in Microwaves and Optics* (IEEE, Copenhagen, Denmark, 2014), pp. 34–36.

[46] A. Momeni, H. Rajabalipanah, M. Rahmanzadeh, A. Abdolali, K. Achouri, V. Asadchy, and R. Fleury, Reciprocal metasurfaces for on-axis reflective optical computing, IEEE Trans. Antennas Propag. **69**, 7709 (2021).

[47] J. Meixner and F. W. Schäfke, *Mathieusche Funktionen und Sphäroidfunktionen* (Springer-Verlag, Berlin, 1954).

[48] L. Schächter, *Beam-wave Interaction in Periodic and Quasi-periodic Structures*, 2nd ed. (Springer, Berlin, 2011).

[49] R.-B. R. Hwang, *Periodic Structures: Mode-matching Approach and Applications in Electromagnetic Engineering* (John Wiley & Sons, Singapore, 2012).

[50] N. W. Mclachlan, *Theory and Application of Mathieu Functions* (Dover, New York, 1964).

[51] S. N. Elaydi, *An Introduction to Difference Equations* (Springer-Verlag, New York, 1999).

[52] G. Minatti, F. Caminita, E. Martini, and S. Maci, Flat optics for leaky-waves on modulated metasurfaces: Adiabatic floquet-wave analysis, IEEE Trans. Antennas Propag. **64**, 3896 (2016).

[53] R. W. P. King and C. W. Harrison, Jr., *Antennas and Waves: A Modern Approach* (MIT Press, Cambridge, Massachusetts, 1969).

[54] R. W. King, The loop antenna for transmission and reception, in *Antenna Theory* Part 1, edited by E. R. Collin and F. J. Zucker (McGraw-Hill, New York, 1969).

[55] K. C. Gupta, R. Garg, I. Bahl, and P. Bhartia, *Microstrip Lines and Slotlines* (Artech House, Boston, 1996).

[56] A. Epstein and O. Rabinovich, Unveiling the Properties of Metagratings via a Detailed Analytical Model for Synthesis and Analysis, Phys. Rev. Appl. **8**, 054037 (2017).

[57] O. Rabinovich and A. Epstein, Analytical design of printed circuit board (PCB) metagratings for perfect anomalous reflection, IEEE Trans. Antennas Propag. **66**, 4086 (2018).

[58] L. Rayleigh, On the dynamical theory of gratings, Proc. R. Soc. London, Ser. A **79**, 399 (1907).

[59] O. Rabinovich, I. Kaplon, J. Reis, and A. Epstein, Experimental demonstration and in-depth investigation of analytically designed anomalous reflection metagratings, Phys. Rev. B **99**, 125101 (2019).

[60] J. C. Rautio, R. L. Carlson, B. J. Rautio, and S. Arvas, Shielded dual-mode microstrip resonator measurement of uniaxial anisotropy, IEEE Trans. Microwave Theory Tech. **59**, 748 (2011).

[61] J. Homola, *Surface Plasmon Resonance Based Sensors* (Springer, Berlin, 2006).